The Astrophysical Journal, 864:63 (15pp), 2018 September 1 https://doi.org/10.3847/1538-4357/aad62d

Broad Non-Gaussian Fe XXIV Line Profiles in the Impulsive Phase of the 2017 September 10 X8.3-class Flare Observed by *Hinode*/EIS

Vanessa Polito[1], Jaroslav Dudík[2], Jana Kašparová[2], Elena Dzifčáková[2], Katharine K. Reeves[1], Paola Testa[1], and Bin Chen[3]
[1] Harvard-Smithsonian Center for Astrophysics, 60 Garden Street, Cambridge, MA 01238, USA
[2] Astronomical Institute of the Czech Academy of Sciences, Fričova 298, 251 65 Ondrejov, Czech Republic
[3] Center for Solar-Terrestrial Research, New Jersey Institute of Technology, Newark, NJ 07102, United States
Received 2018 July 5; revised 2018 July 24; accepted 2018 July 24; published 2018 August 30

Abstract

We analyze the spectra of high-temperature Fe XXIV lines observed by the *Hinode*/Extreme-Ultraviolet Imaging Spectrometer (EIS) during the impulsive phase of the X8.3-class flare on 2017 September 10. The line profiles are broad, show pronounced wings, and clearly depart from a single-Gaussian shape. The lines can be well fitted with κ distributions, with values of κ varying between ≈1.7 and 3. The regions where we observe the non-Gaussian profiles coincide with the location of high-energy (≈100–300 keV) hard X-ray (HXR) sources observed by *RHESSI*, suggesting the presence of particle acceleration or turbulence, also confirmed by the observations of nonthermal microwave sources with the Expanded Owens Valley Solar Array at and above the HXR loop-top source. We also investigate the effect of taking into account κ distributions in the temperature diagnostics based on the ratio of the Fe XXIII λ263.76 and Fe XXIV λ255.1 EIS lines. We found that these lines can be formed at much higher temperatures than expected (up to $\log(T[\mathrm{K}]) \approx 7.8$) if departures from Maxwellian distributions are taken into account. Although larger line widths are expected because of these higher formation temperatures, the observed line widths still imply nonthermal broadening in excess of $200\,\mathrm{km\,s^{-1}}$. The nonthermal broadening related to HXR emission is better interpreted by turbulence than by chromospheric evaporation.

Key words: line: profiles – radiation mechanisms: nonthermal – Sun: activity – Sun: flares – Sun: UV radiation – techniques: spectroscopic

1. Introduction

Solar flares (e.g., Fletcher et al. 2011; Schmieder et al. 2015) are bright manifestations of the release of magnetic energy via the process of magnetic reconnection, leading to a plethora of observed dynamics. From the viewpoint of spectroscopy, one of the long-standing problems is the presence of broad profiles of flare lines, usually interpreted in terms of nonthermal (turbulent) velocities (e.g., Doschek et al. 1979, 1980; Feldman et al. 1980; Culhane et al. 1981; Antonucci et al. 1982, 1986; Tanaka et al. 1982; Antonucci 1989; Landi et al. 2003; Del Zanna et al. 2006; Milligan 2011; Brosius 2013; Young et al. 2013; Tian et al. 2014; Polito et al. 2015; Polito et al. 2016; Bamba et al. 2017; Lee et al. 2017; Woods et al. 2017). Typically, the largest nonthermal velocities, of the order of 100–200 $\mathrm{km\,s^{-1}}$, are observed in the hottest flare lines available, such as Fe XXI–Fe XXVI. Such high nonthermal broadenings occur exclusively during the start or the impulsive phases of a flare, followed by a decrease to about 60 $\mathrm{km\,s^{-1}}$ during the gradual phase. Reports of much smaller velocities of ≈40 $\mathrm{km\,s^{-1}}$ in the impulsive phase have also been made (Young et al. 2015, Table 2 therein) using the Fe XXI line observed by the *IRIS* satellite (De Pontieu et al. 2014). Progressive broadenings, from about 40 to 90 $\mathrm{km\,s^{-1}}$, have also been reported during the rise phase of a long-duration X1-class flare (see, e.g., Section 3.2 and Figure 10 of Dudík et al. 2016). If the broad flare line profiles are interpreted in terms of the equivalent (Doppler) ion temperatures, values above 100 MK can be obtained (e.g., Antonucci et al. 1986; Antonucci 1989), which are almost an order of magnitude higher than the corresponding electron temperatures of several $\times\ 10^7$ K at which the hot flare lines are formed.

For the sake of completeness, we note that nonthermal broadening of EUV lines of the order of several tens of kilometers per second are found also outside flaring regions, such as in the active region (AR) transition region and corona (e.g., De Pontieu et al. 2015; Brooks & Warren 2016; Testa et al. 2016). Further, large nonthermal velocities are not found exclusively in flares, but can also be found in microflares, where they can also reach 145 $\mathrm{km\,s^{-1}}$ (Brosius 2013, Table 2 therein).

Recently, Jeffrey et al. (2016, 2017) showed that the shape of the broad line profiles during flares can deviate from a single Gaussian. In particular, non-Gaussian wings were observed in the Fe XVI and Fe XXIII lines with the Extreme-Ultraviolet Imaging Spectrometer (EIS; Culhane et al. 2007) on board the *Hinode* spacecraft (Kosugi et al. 2007). These line profiles were fitted by the non-Maxwellian κ-distributions (Olbert 1968; Vasyliunas 1968a, 1968b; Livadiotis & McComas 2009; Dudík et al. 2017a; Livadiotis 2017), yielding low values of κ (≈2–3), which indicate strong departures from the Gaussian shape. We note that similar findings were obtained for AR brightenings in transition region lines (Dudík et al. 2017b), as well as coronal holes (Jeffrey et al. 2018). Jeffrey et al. (2017) found that the flare line profiles described by a κ-distribution could occur as a result of either ion acceleration or the presence of turbulence. This is not surprising, since turbulence leads naturally to enhanced high-energy tails of the particle distributions, if the turbulent diffusion coefficient is inversely proportional to velocity (Hasegawa et al. 1985; Laming & Lepri 2007; Che & Goldstein 2014). In flares, such a situation can lead to a κ-distribution (Bian et al. 2014). The high-energy tails can, however, also be produced by particle acceleration (e.g., Gontikakis et al. 2013; Gordovskyy et al. 2013, 2014) or

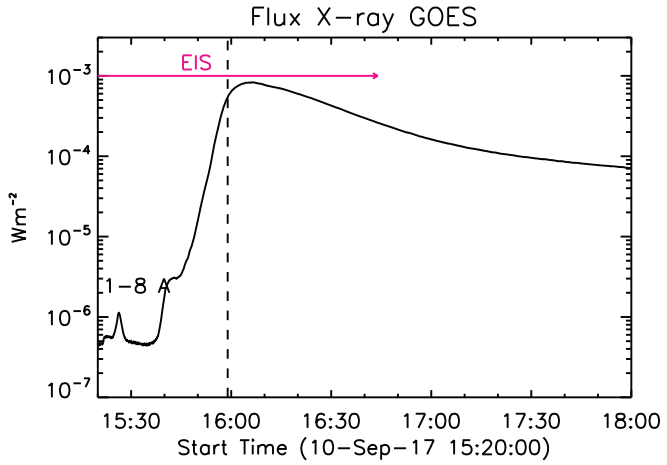

Figure 1. *GOES* soft X-ray light curve in the 1–8 Å channel for the X-class flare on 2017 September 10. The pink arrow indicates the duration of the EIS observation under study (which starts at 05:44 UT). The horizontal dotted line shows the time where we observe the non-Gaussian Fe XXIV line profiles.

wave–particle interaction involving whistler waves, as shown by Vocks et al. (2008, 2016).

The κ-distributions of electrons have been suggested in flares using the *RHESSI* (Lin et al. 2002) spacecraft. The method consisted of fitting the X-ray bremsstrahlung spectra, which allows us to determine the κ index for the high-energy tail (Oka et al. 2013, 2015) or the entire spectrum (Kašparová & Karlický 2009). Alternatively, the κ parameter can be determined by combining observations from the *RHESSI* spacecraft and the Atmospheric Imaging Assembly (AIA; Boerner et al. 2012; Lemen et al. 2012) on board the *Solar Dynamics Observatory* (*SDO*; Pesnell et al. 2012) using the mean electron flux spectrum (Battaglia & Kontar 2013; Battaglia et al. 2015). Yet another method involves the ratios of emission-line intensities that are formed over a wide range of energies of the impacting electrons that produce ionization and excitation. Such a method has been used to detect strongly non-Maxwellian κ-distributions in the rise and impulsive phases of the X5.4-class solar flare of 2012 March 07 (Dzifčáková et al. 2018).

In this work, we report on detection of strongly non-Gaussian and broad-line profiles of Fe XXIV at the top of the flare loops during the strongest solar flare of solar cycle 24, i.e., the X8.3-class flare of 2017 September 10. This is a limb flare, allowing for localizing the non-Gaussian profiles from a different viewpoint than the on-disk flares of Jeffrey et al. (2016, 2017). The paper is organized as follows. Section 2 describes the spectroscopic observations used and their reduction. Fitting of the line profiles is detailed in Section 3, and the results on temperature diagnostics based on the Fe XXIV λ255.10/Fe XXIII λ263.76 ratio are discussed in Section 4. Section 5 describes the analysis of the *RHESSI* spectra and fitting of the various spectral components. The results obtained are discussed in Section 6, and a summary is given in Section 7.

2. Observations

The X8.3 flare under study occurred on 2017 September 10 in the AR $\beta\gamma$ NOAA 12673 on the west limb of the Sun. The flare started at ≈15:40 UT and peaked at about 16:06:28 UT, as observed by the *GOES* satellite in the 1–8 Å filter (see Figure 1). Several authors have focused on the analysis of this event, which was observed simultaneously by different satellites, including *SDO*, *Hinode*, *IRIS*, *RHESSI*, and *Fermi* (e.g., Li et al. 2018; Long et al. 2018; Seaton & Darnel 2018; Warren et al. 2018; Yan et al. 2018; Liu et al. 2018). The flare was initiated by a fast eruption of a flux rope cavity starting at about 15:54UT. It was also associated with an increase in nonthermal electron energy flux as measured by *Fermi* (see Figure 1 in Long et al. 2018). Spectroscopic observations performed by *Hinode*/EIS were studied in Warren et al. (2018) and Li et al. (2018), who focused on studying the evolution of the hot plasma in a plasma sheet formed after the fast eruption and above the flare loops, from Solar-X coordinates ≈960″ toward larger solar radii (see Figure 2).

In this work, we focus on analyzing the profiles of the high-temperature lines observed by *Hinode*/EIS (Fe XXIV and Fe XXIII) in the plasma sheet at around 15:59 UT, as indicated by the horizontal line in Figure 1. We note that Warren et al. (2018) and Li et al. (2018) focused on the EIS spectra observed after 16:09 UT, i.e., toward the peak and gradual phases of the flare. At these times, the Fe XXIV and Fe XXIII lines could be well fitted by Gaussians (see, e.g., Figure 2 in Li et al. 2018; Figure 10 in Warren et al. 2018). Long et al. (2018) studied the EIS spectra associated with the fast eruption at about 15:42 and 15:54 UT (see their Figures 3 and 4). Our analysis is complementary to these ones both in time and because of its different focus on the non-Gaussian shape of line profiles.

The analysis of the EIS spectra is complicated by some well-known technical issues (as summarized on the EIS wiki page[4]), some of which are briefly described in Section 2.1. We use high-resolution *SDO*/AIA images (0.″6 per pixel) in the 193 Å filters, which provide an essential context for the spectroscopic observations and useful information on the plasma emission measure (see Section 4). The level 1.5 AIA data were processed using the *SolarSoft* (SSW; Freeland & Handy 1998) routine `aia_prep.pro`, which corrects for instrumental pointing errors and co-aligns images from different filters on a common platescale. We also analyzed hard X-ray (HXR) images from the *RHESSI* satellite, whose data reduction is discussed in Section 5. The flare was also observed in microwave wavelengths in 2.5–18 GHz by the Expanded Owens Valley Solar Array (EOVSA). An overview of the EOVSA observations is provided by Gary et al. (2018).

2.1. EIS Data Reduction and Instrumental Issues

On 2017 September 10 EIS observed the AR 12673 while running a large 80-step raster from 05:44 UT to 16:44 UT, covering all the impulsive and part of the gradual phase of the X8.3-class flare (see Figure 1). For each raster, the 80 2″ slit positions were separated by a 1″ jump, resulting in a 3″ raster step and a field of view for the spectrometer of 240″ × 304″. The exposure time was 5 s, and the total duration of each raster was ≈535 s. The EIS study consisted of 15 spectral windows, which included three high-temperature lines that are only observed during flares: Fe XXIII λ263.76 ($\log(T\,[\mathrm{K}]) \approx 7.15$) and Fe XXIV $\lambda\lambda$192.03 and 255.10 ($\log(T\,[\mathrm{K}]) \approx 7.2$). The Fe XXIII λ263.76 line is believed to be largely free of blends, whereas the Fe XXIV $\lambda\lambda$192.03 and 255.10 lines are contaminated with unidentified emission at 1 MK, as well as other lines including Fe XI, Fe XII, Fe XVII (Del Zanna 2008, 2012),

[4] http://solarb.mssl.ucl.ac.uk/eiswiki/Wiki.jsp?page=EISAnalysisGuide

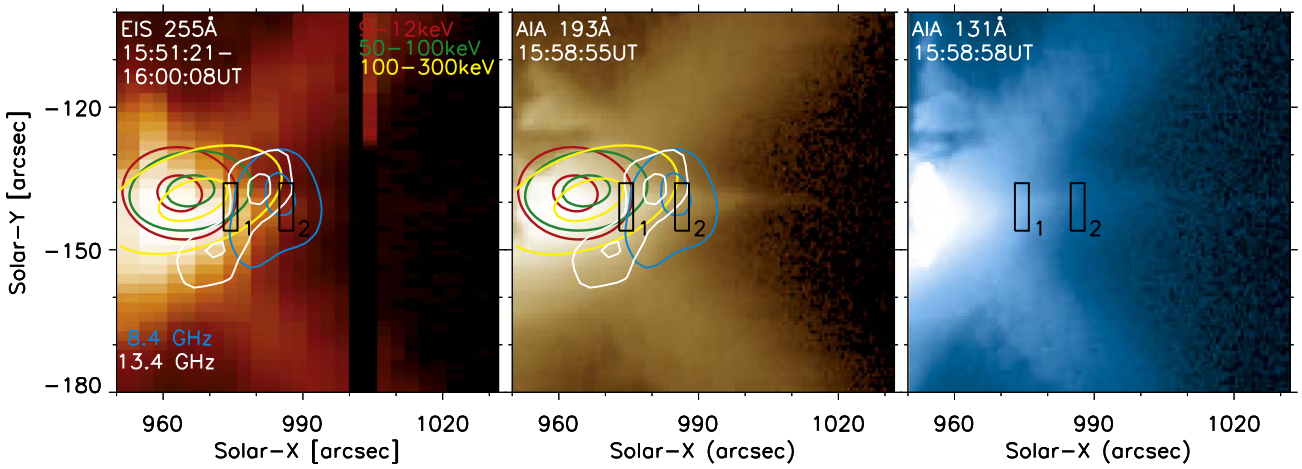

Figure 2. Overview of the 2017 September 10 flare observation with *Hinode*/EIS and *SDO*/AIA. Left panel: intensity image formed in the Fe XXIV λ255.10 line during one of the EIS rasters (from 15:51:21 to 16:00:08 UT), obtained by performing a single-Gaussian fit at each raster pixel. Middle and right panels: AIA 193 Å and 131 Å images at the closest time to the EIS raster exposure numbers 8–9. The colored contours in the left and middle panels show 50% and 90% of the maximum intensity of the HXR sources observed by *RHESSI* during the time interval 15:58:40–15:59:40 UT, and the microwave sources observed by EOVSA between 15:59:08 UT and 15:59:12 UT, with different colors indicating different energy intervals as shown in the legend. Finally, black boxes 1 and 2 indicate the location where we perform the κ fitting of the Fe XXIV λ255.10 (raster exposures 8–9) and λ192.03 (raster exposures 12–13) lines, respectively.

especially if the width of the Fe XXIV lines is large. Nevertheless, during flares, Fe XXIV appears to be the dominant contribution (Del Zanna 2008).

The level 0 EIS data were converted to level 1 datacubes (λ, *X*-pixels, *Y*-pixels) by using the `eis_prep.pro` routine with some of the standard options,[5] including the keyword `refill` to interpolate the missing pixels. We note that the interpolation is a necessary step because of the large number of missing pixels in this observation. According to the EIS Software Note 13, the interpolation works well since the EIS spatial resolution is 3–4 pixels in the solar *Y* direction. This means that a signal within a given pixel contains a significant component from the neighboring spatial element. We also note that the interpolation of EIS spectra is a standard procedure before non-Gaussian fitting (see Section 4.7 of Jeffrey et al. 2016; see also Jeffrey et al. 2017, 2018). However, in some cases our profiles still show one or two missing pixels that could not be interpolated by `eis_prep.pro`. Finally, because of the uncertainty in the EIS radiometric calibration and its evolution (see, e.g., Del Zanna 2013; Warren et al. 2014), we use the `/noabs` keyword in `eis_prep.pro` and obtain the spectra in data number (DN).

We estimated an offset of about 16.5 pixels between the short-wavelength (SW, including the Fe XXIV λ192.03 line) and long-wavelength (LW, including the Fe XXIV λ255.10 line) CCD channels by using the routine `eis_ccd_offset.pro`. Although we took into account this offset when co-aligning spectra from the two CCDs, for simplicity the spectra are labeled with their original "uncorrected" pixel position. We also note that because of the offset between the two CCDs and the fact that the instrumental width varies with the CCD *Y*-pixel position, the latter will be different for lines that are included in different CCD channels, such as the Fe XXIV $\lambda\lambda$192.03 and 255.10 (or Fe XXIII λ263.76) lines. This difference needs to be taken into account when fitting the line profiles, as discussed in Section 3. Further, we correct for the spectral tilt by using the SSW routine `eis_slit_tilt_array.pro`.

[5] ftp://sohoftp.nascom.nasa.gov/solarsoft/hinode/eis/doc/eis_notes/01_EIS_PREP/eis_swnote_01.pdf

Finally, Warren et al. (2018) pointed out the effects of the EIS asymmetric point-spread function, which causes apparent red- and blueshifts in the centroid of the Fe XXIV line (and other bright lines) on either side of the plasma sheet for the flare under study (see Figure 12 of Warren et al. 2018). We note that this instrumental effect does not influence the result of our analysis, as we observe Fe XXIV spectra with pronounced wings in several locations across the plasma sheet in the direction perpendicular to its length. In addition, if this effect was responsible for creation of the non-Gaussian wings, it should be seen in other conditions, for example, in the same lines at different times. This is not the case, as these strong lines become Gaussian after 16:09 UT (Li et al. 2018; Warren et al. 2018).

3. Fitting of the Fe XXIV and Fe XXIII Lines

Mostly symmetric Fe XXIV line profiles with pronounced wings were observed at several locations along the plasma sheet feature during the EIS raster that was running between 15:51 UT and 16:00:08 UT. The left panel of Figure 2 shows the intensity map of the EIS Fe XXIV λ255.10 line during this raster, which has been obtained by performing an approximate single-Gaussian fit at each pixel location. We note that the EIS slit rasters from right to left, and therefore the intensity map is actually a composite image obtained at different times. The profiles that we analyze in this work are observed in boxes 1 and 2 (shown in Figure 2), whose locations correspond respectively to the *X*-pixels 8–9 and 12–13 of the EIS datacube. Boxes 1 and 2 are located above the loop tops, at the bottom and along the plasma sheet structure, respectively. The right panel shows the AIA 193 Å image at ≈15:59 UT, which is the approximate time where the EIS slit was rastering the location indicated by box 1. Overlaid on both images in the left and right panels are the contours of *RHESSI* sources at different energy intervals, as indicated by the legend on the top right. The contour levels show 50% and 90% of the maximum intensity of the *RHESSI* images, which are integrated over the interval 15:58:40–15:59:40 UT by using the standard image reconstruction algorithms (see Section 5). The *RHESSI* sources

show the presence of very energetic electrons (above 100 keV) and coincide with the loop top of the flare, suggesting that we are observing a coronal HXR source. Such a bright coronal source cannot be interpreted in the standard thin-target scenario, but it shows properties similar to some of the coronal hard X-ray sources discussed in, e.g., Krucker et al. (2008, and references therein). Note that there is also a *RHESSI* footpoint source outside the field of view of Figure 2, which is detectable above ≈30 keV (see Gary et al. 2018). Figure 2 also shows a microwave source observed by EOVSA between 15:59:08 UT and 15:59:12 UT. This source is located at and above the HXR loop-top source, with a characteristic nonthermal gyrosynchrotron spectral shape and a maximum brightness temperature of over 3×10^9 K, suggesting the presence of highly energetic, mildly relativistic electrons in the loop-top region.

The Fe XXIV λ255.10 line is intense enough in the location of box 1 that the fitting of the spectra (in particular the line wings) can be reliably performed. This location coincides well with the contours of the *RHESSI* high-energy sources. The line is saturated on the left side of box 1 and too faint on its right side. On the other hand, the Fe XXIV λ192.03 line is saturated where the *RHESSI* sources are most intense, and we can reliably fit the line only in the region indicated by box 2. Although the saturation threshold of EIS is around 1.5×10^4 DN, we believe that nonlinear effects in the instrumental gain might be important below this value, resulting in an underestimation of the peak for very intense lines. For this reason, we do not analyze line profiles with peak intensities above $\approx 10^4$ DN. We also only select profiles where the interpolation algorithm has removed most of the missing pixels, with the exception of a maximum of two pixels.

To fit the Fe XXIV λλ255.10 and 192.03 lines, we use either a single (or multiple) Gaussian or a κ fit, the latter performed by using the method described in Section 2.3 of Dudík et al. (2017b). In particular, we perform a convolution of the EIS instrumental Gaussian profile and a κ profile by using a modified version of the SSW `comp_gauss.pro` routine. This convolution has the form (see Jeffrey et al. 2016, 2017)

$$I(\lambda) = I_0 \int_{-\infty}^{\infty} e^{-\frac{(\lambda-\lambda')^2}{2w_{\rm instr}^2}} \left(1 + \frac{(\lambda' - \lambda_0)^2}{2(\kappa - 3/2)w_\kappa^2}\right)^{-\kappa} d\lambda', \quad (1)$$

where I_0 is the peak intensity, λ_0 is the wavelength of the line center, w_κ is the characteristic width, and κ is the non-Maxwellian parameter.

As mentioned in Section 2.1, the EIS instrumental width $w_{\rm instr}$ varies between the two Fe XXIV lines, and it is estimated to be ≈0.0704 and 0.0698 Å for the λλ192.03 and 255.10 lines, respectively, as calculated using the SSW routine `eis_slit_width.pro`.

For both the Gaussian and κ fits, the weights W are given by

$$W = \sqrt{\frac{1}{\sigma^2(I(\lambda_i))}}, \quad (2)$$

where $\sigma(I(\lambda_i))$ are the intensity errors obtained from `eis_prep.pro`, which take into account the photon statistics noise, pedestal, and error of the dark current.

To evaluate the goodness of fit, we use the reduced $\chi^2_{\rm red}$ (e.g., Equation (18) of Dudík et al. 2017b), as well as the residuals R of the fits, obtained as

$$R = I_{\rm obs}(\lambda_i) - I_{\rm fit}(\lambda_i), \quad (3)$$

where $I_{\rm obs}$ and $I_{\rm fit}$ are the observed spectra and fit, respectively, for each wavelength λ_i. Note that in the following sections we will mostly express the width of the fitted lines in terms of characteristic widths $w_{\rm G}$ or w_κ as obtained from either the Gaussian or κ fit, respectively. In order to convert from w_κ to FWHM_κ, we use Equation (14) of Dudík et al. (2017b), which we recall here for the reader's convenience:

$$w_\kappa = \frac{1}{8} \frac{\mathrm{FWHM}_\kappa}{(\kappa - 3/2)(2^{1/\kappa} - 1)}. \quad (4)$$

For the Gaussian fit, $w_{\rm G}$ is simply equal to

$$w_{\rm G} = \frac{\mathrm{FWHM}_{\rm G}}{\sqrt{8 \ln 2}}. \quad (5)$$

The fitting procedures for the Fe XXIV λλ255.10 and 192.03 lines are discussed separately in Sections. 3.1 and 3.2.

3.1. Fe XXIV λ255 Line Fitting

Figure 3 shows two examples of Fe XXIV λ255.10 spectra at X-pixels = 9 and Y-pixels = 210 and 211 within box 1, which have been fitted with a single κ (left panel) and Gaussian (right panel) function. The results of the fit ($\chi^2_{\rm red}$ value, κ value, and line width expressed in Å, with corresponding errors) are indicated in the same panels. At the bottom of both panels, we show the fitting residuals along the spectra (see Equation (3)). We found that in both cases the single κ fit performs much better than the Gaussian one, with considerably lower values of $\chi^2_{\rm red}$ and residuals. The same result is obtained for all the "good" pixels in box 1 (≈10) that we selected according to the criteria described above, as also discussed in Section 6. We note that the red wing of the line is partially outside the spectral window, whereas the blue wing can be properly fitted. The fact that part of the spectrum is missing can potentially create some problems in the convolution part of the fitting algorithm. To rule this out, we compared the results of the convolution (Equation (1)) and fit with a purely κ-profile (Dudík et al. 2017b),

$$I(\lambda) = I_0 \left(1 + \frac{(\lambda - \lambda_0)^2}{2(\kappa - 3/2)w_\kappa^2}\right)^{-\kappa} d\lambda, \quad (6)$$

and we verified that there is no significant difference (within the uncertainties) between the κ and line width values estimated using the convolution or purely κ fit. This is not surprising, since the lines are much broader than the EIS instrumental width. As discussed in Dudík et al. (2017b), the pronounced wings can also be reproduced by a combination of two Gaussian profiles, which can be interpreted as the superposition of emission from plasma formed at two different temperatures. To investigate this possibility, we performed a double-Gaussian fit of the Fe XXIV λ255.10 line in the same pixels of box 1. Since the spectrum is missing its red wing, in most cases the uncertainties of the two-component fits were too high (with a $\chi^2_{\rm red}$ value much less than 1), except from one pixel (raster exposure 8, Y-pixel 210). Figure 4 shows the comparison of the κ, Gaussian, and double-Gaussian fit for this single case. The FWHMs obtained from the double-Gaussian fit (using Equation (5)) are of the order of 0.20 and 0.34 Å for

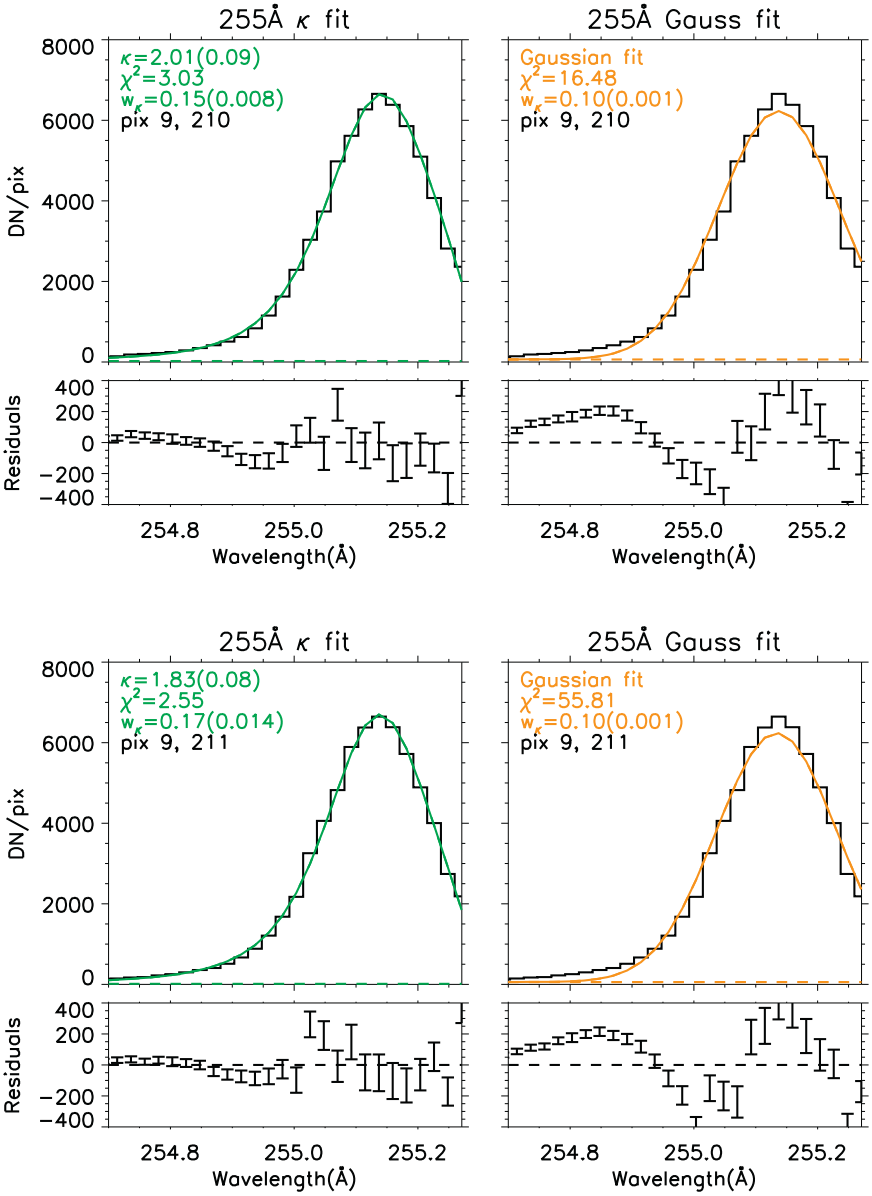

Figure 3. Example of κ (left panels) and single-Gaussian (right panels) fits of the EIS Fe XXIV λ255.10 line during raster exposure 9 and slit pixels 210 and 211 (top and bottom panels, respectively) inside box 1 of Figure 2. For each fit, the value of χ^2 is indicated in the upper left part of the panel, as well as the width of the line obtained by the fit and its uncertainty. For the κ fit, also the value of κ and the associated error are shown.

the two Gaussian components, which can be used to estimate the required nonthermal velocity as follows:

$$v_{\rm nth} = \frac{c}{\lambda_0}\frac{1}{2\sqrt{\ln 2}}\sqrt{(w^2 - w_{\rm instr}^2 - w_{\rm th}^2)}. \quad (7)$$

Using the equation above, we can estimate that the line width of the broader Gaussian component corresponds to very large nonthermal velocities (of the order of $\approx$300 km s^{-1}). Although we cannot completely rule out the possibility of fitting the large wings with two Gaussian components, a single κ fit appears as a possible simple explanation to account for the non-Gaussian shape of the line. Note that the line width obtained from the κ fit ($\approx$0.10 Å; see Figure 4) corresponds to an FWHM$_\kappa$ of 0.19 Å (using Equation (4)) and thus to a lower value of nonthermal velocity ($\approx$150 km s^{-1}).

3.2. Fe XXIV λ192 Line Fitting

The Fe XXIV λ192.03 line is the most intense of the observed EIS flare lines, as its centroid is close to the peak of sensitivity of the spectrometer. Unfortunately, the line was saturated in box 1, where the *RHESSI* HXR sources are located. Nevertheless, the line could be reliably observed in the region indicated by box 2 in Figure 2, which is also located along the plasma sheet feature. In contrast to the Fe XXIV λ255.10 line, both wings can be observed in the λ192.03 spectrum. In most pixels of box 2, the line shows the presence of a blend in the red wing and possibly a less intense one in the blue wing. The origin of both these blends is unclear. One may think that the blend on the red wing of the Fe XXIV λ192.03 line might be due to the Fe XII transition at 192.39 Å. To investigate this possibility, we estimate the predicted intensity of the Fe XII λ192.39 line by measuring the intensity of another

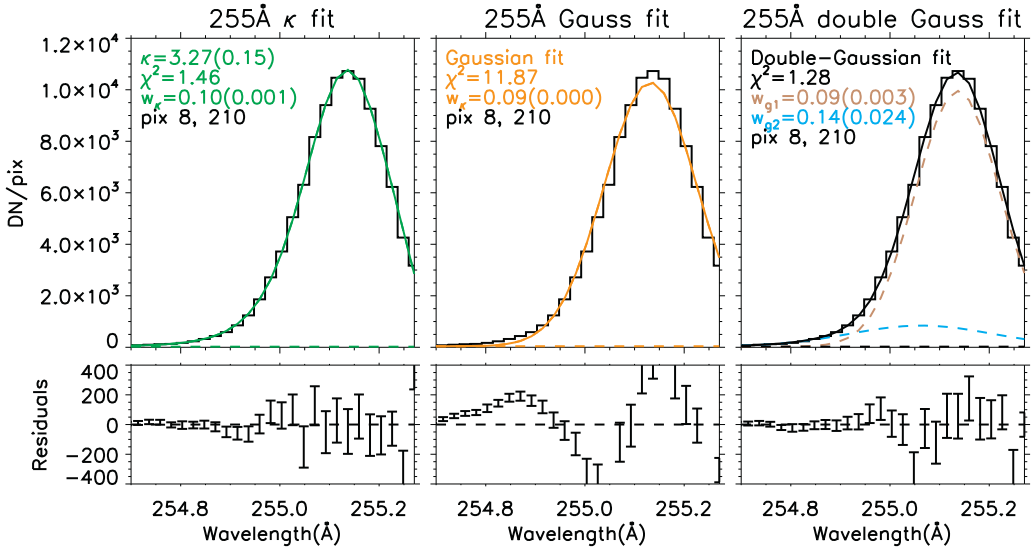

Figure 4. Example of κ (left panel), single-Gaussian (middle panel), and double-Gaussian (right panel) fits for the EIS Fe XXIV λ255.10 line during raster exposure (X-pixel) 8 and slit Y-pixel 210 (box 1 of Figure 2). See Figure 3 caption and the text for more details.

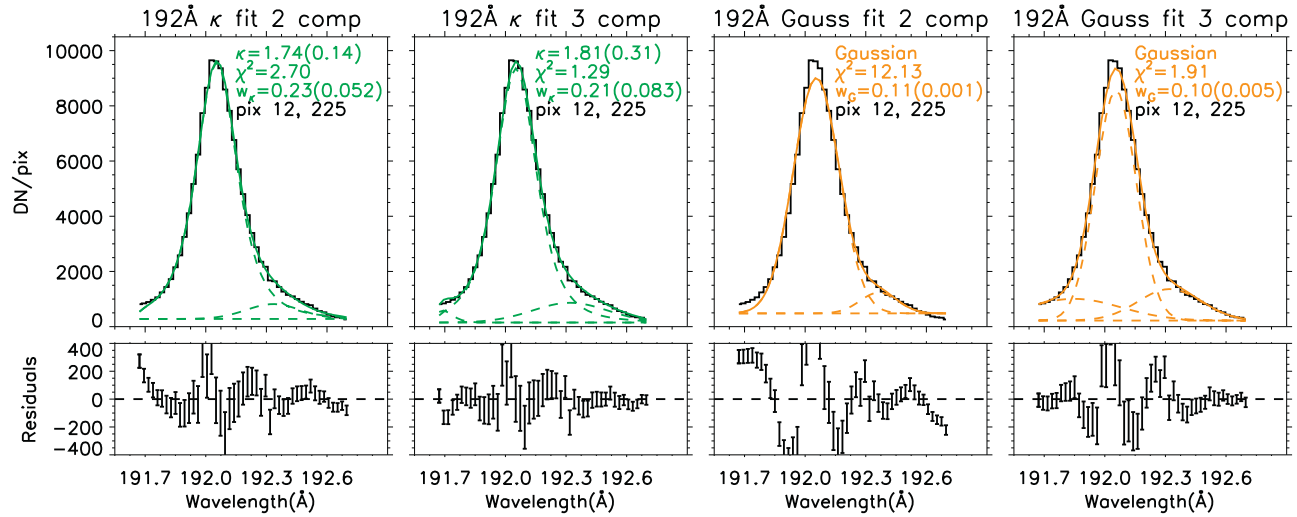

Figure 5. From left: example of κ fit and Gaussian fit with one or two blends for the EIS Fe XXIV λ192.03 line during raster exposure 12 and slit pixel 225 (box 2 of Figure 2). See Figure 3 caption for more details.

Fe XII transition at 186.88 Å and using the theoretical ratio of these two lines from CHIANTI. We find that the predicted intensity of the Fe XII λ192.39 line is significantly lower (by a factor of $\approx$50) than the intensity of the observed blend on the red side of the Fe XXIV λ192.03 line, and we can thus rule out this interpretation. Another possible explanation may be that we are observing an unknown transition or a redshifted component of the Fe XXIV λ192.03 line. Such a redshifted component might not be observed in the Fe XXIV λ255.10 spectra, as in that case the line partially lies outside the spectral window.

Figure 5 shows an example of the Fe XXIV λ192.03 spectrum at raster exposure (or X-pixel) 12 and Y-pixel 225, which corresponds to Y-pixels $\approx$208–209 for the Fe XXIV λ255.10 observation, considering the offset of $\approx$16.5 pixels between the SW and LW channels. The four panels of Figure 5 show the results of different fitting procedures that we applied to the same spectrum (from left to right): a κ fit with one or two blends and a Gaussian fit with one or two blends. It should be noted that the blends in the κ fit are assumed to be Gaussian, because their intensity lines are too low to determine the shape of their profiles, as well as to limit the number of free parameters of the fit. Figure 5 shows that a κ distribution plus only one blend on the red wing of the line provides a very good fit of the observed spectrum, without the need of adding an extra component on the blue side of the Fe XXIV line. This is not the case for the Gaussian fit, where two extra components are required. These components also need to be very large to properly fit the line profile, resulting in a width for the Fe XXIV line that is narrower than the ones observed for the Fe XXIV λ255.10 and Fe XXIII λ263.76 lines, as shown in Figure 6. While the last two lines are too faint to perform a reliable fit of their wings (see the $\chi^2_{\rm red}$ value well below 1), their $\mathrm{FWHM_G}$ values are estimated from the Gaussian fit to be around 0.30 Å for the Fe XXIV λ255.10 line and 0.27 Å for the lower-temperature Fe XXIII λ263.76 line (corresponding to $w_{\rm G} = 0.13$ and 0.12 Å, respectively), as indicated in Figure 6. It is reasonable to assume that the width of the Fe XXIV λ192.03 line would be at least as large as the width of the other Fe XXIV line. However, if we fix the minimum $\mathrm{FWHM_G}$ of the Fe XXIV λ192.03 line to be at least equal to a conservative value

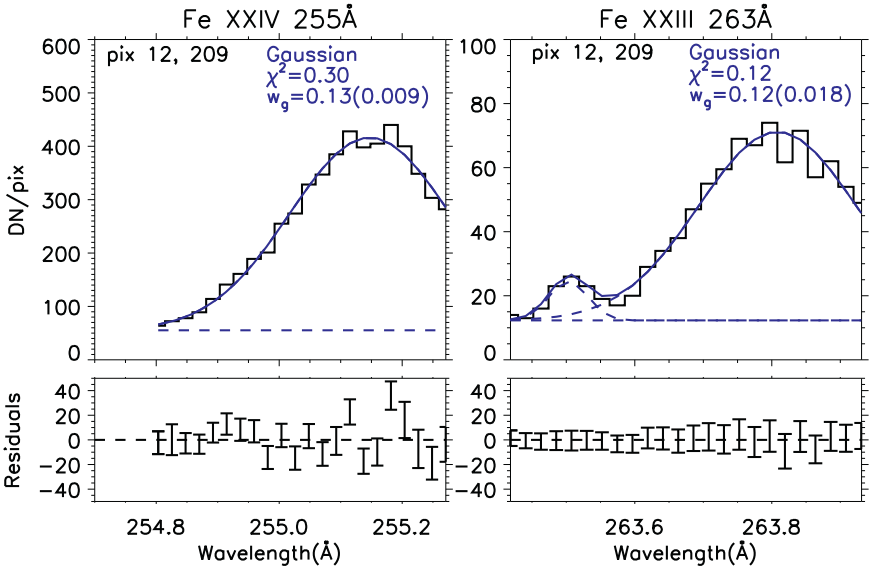

Figure 6. Sample spectra of the Fe XXIV λ255.10 (left panel) and Fe XXIII λ263.76 (right panel) lines for raster exposure 12, *Y*-pixel 209 for the LW detector (corresponding to *Y*-pixel ≈225 in the SW detector). The spectra show that the lines are quite broad at this location, with w_G equal to 0.13 ± 0.009 Å (or $FWHM_G = 0.030 \pm 0.02$ Å) for the Fe XXIV λ255.10 line.

of 0.26 Å (or equivalently $w_G = 0.11$ Å) in the three-component Gaussian fit, the latter does not perform as well, with a value of χ^2_{red} and residuals that are significantly larger than those obtained for the three-component κ fit (see Figure 7). We consider this an additional indication that the Fe XXIV λ192.03 line, even if blended, is best fitted with a κ rather than a Gaussian profile.

The κ values obtained from fitting the Fe XXIV $\lambda\lambda$192.03 and 255.10 lines are summarized in Figure 8, assuming two (i.e., one line blend; left panel) or three components (i.e., two line blends; right panel) for the fit of the λ192.03 line.

4. Temperature Diagnostics Based on the Fe XXIV λ255.10/Fe XXIII λ263.76 Ratio

We use the ratio of the Fe XXIV λ255.10 and Fe XXIII λ263.76 lines to estimate the *electron* temperature T_e of the emitting plasma in the location indicated by box 1 in Figure 2 at around 15:59 UT. We convert the Fe XXIV and Fe XXIII intensities from DN to physical units (i.e., photons s^{-1} cm^{-2} $arcsec^{-1}$) using the radiometric calibration of Del Zanna (2013). As mentioned in Section 2.1, the EIS radiometric calibration may need to be revised to take into account the instrument degradation after 2014. Nevertheless, problems in the calibration should not affect our results dramatically, as we use lines that are close in wavelength and are included in the same CCD detector. We find that the ratio estimated using the radiometric calibration from Del Zanna (2013) (≈12.1) is very similar to the one obtained using the ground calibration (≈12.8). This is not surprising, as the correction factor shown in Del Zanna (2013) appears to be similar in the wavelength interval around 250–260 Å (see middle panel of Figure 8 of Del Zanna 2013). We note that the in-flight calibration produces only a difference of ≈0.02 in the resulting log(*T*[K]) estimated from the Fe XXIV λ255.1/Fe XXIII λ263.8 line intensity ratio. A ratio of 12.1 indicates a temperature of log(*T*[K]) 7.44 in the Maxwellian case (see the right panel of Figure 9).

We also investigated the effect of taking into account non-Maxwellian conditions in the local plasma on the temperature

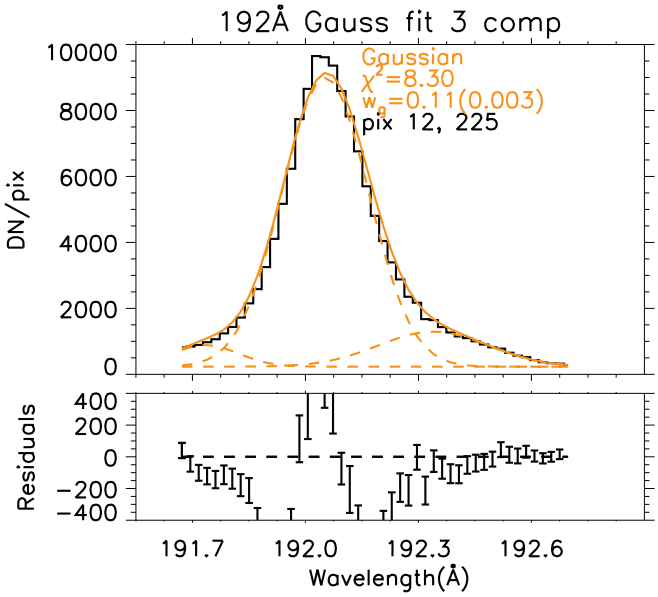

Figure 7. Gaussian fit with two blends for the EIS Fe XXIV λ192.03 line during raster exposure 12 and slit *Y*-pixel 225 (box 2 of Figure 2), obtained by fixing the minimum value of the line width to w_G of around 0.11 Å (or $FWHM_G$ of 0.026 Å; see the text for more details).

diagnostic. The left panel of Figure 9 shows the fractional ion abundance of the Fe XXIII and Fe XXIV lines for the Maxwellian and κ-distributions with different values of κ, as obtained using the KAPPA package (Dzifčáková et al. 2015) and CHIANTI v8. We note that these ionization equilibria were obtained by assuming *electron* κ-distributions, which may not necessarily be the same as *ion* distributions (see Section 7.1 of Dudík et al. 2017b, as well as our Section 6). We note that the peak formation temperature of the Fe XXIII and Fe XXIV lines is strongly shifted to higher values for decreasing values of κ. In turn, the calculated Fe XXIV λ255.10/Fe XXIII λ263.76 ratios as a function of different κ, shown in the right panel of Figure 9, are also shifted to higher T_e (see Dzifčáková et al. 2018). The

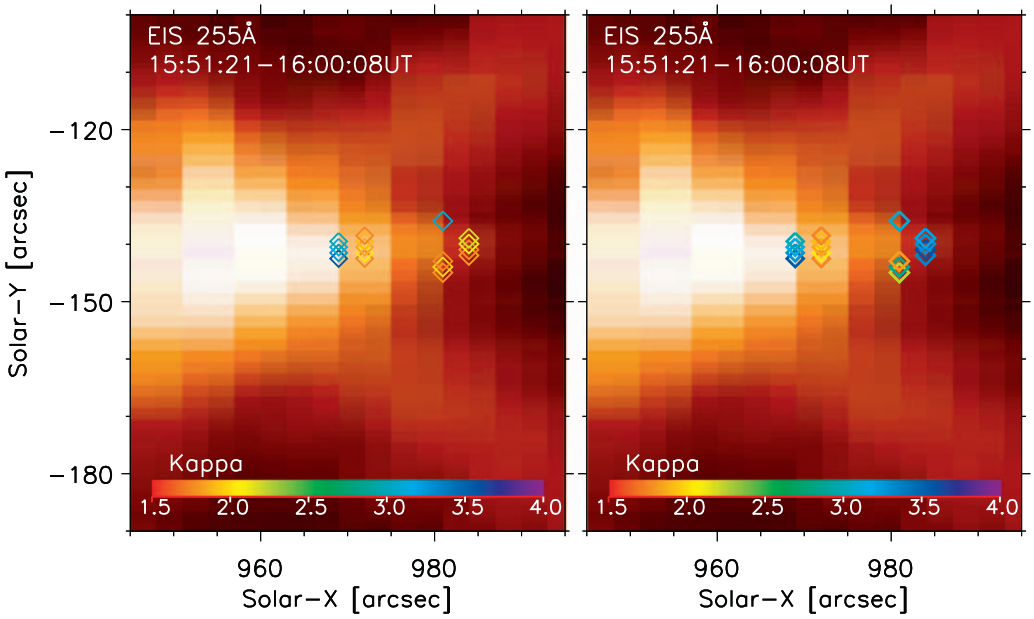

Figure 8. Distribution of κ values obtained by fitting the Fe XXIV λ255.10 and Fe XXIV λ192.03 lines overlaid on intensity images formed in the EIS Fe XXIV λ255 line. The fit of the Fe XXIV λ192.03 line includes one or two blends (left and right panels, respectively).

horizontal blue line in this panel indicates the observed ratio in box 1. Figure 9 shows that the temperature diagnostic varies significantly with κ, from $\log(T_e\,[\mathrm{K}]) \approx 7.44$ for Maxwellian to 7.82 for $\kappa = 2$; see the dot-dashed lines in the right panel of Figure 9. In particular, using the average value of κ obtained from the fit of the Fe XXIV λ255.10 spectra in box 1 ($\approx$2–3; see Section 3.1 and Figure 8), we estimate a temperature of the hot plasma at the plasma sheet feature of the X-class 2017 September 10 flare to be between $\log(T_e[\mathrm{K}]) = 7.6$ and 7.8. This value is significantly higher than the corresponding Maxwellian one (see also Warren et al. 2018, Figures 5–6 therein), by a factor of $\approx$2.4 for $\kappa = 2$. These results are in line with the non-Maxwellian temperature diagnostics of Dzifčáková et al. (2018).

We also note that the diagnosed temperatures are above the corresponding ionization peaks of Fe XXIV independently of whether the conditions are Maxwellian or non-Maxwellian. Such high temperatures have been reported before (Tanaka et al. 1982), and in the context of our observation, they suggest that the presence of cool line blends (such as Fe XVII; e.g., Del Zanna 2008) on the wings of the Fe XXIV lines is unlikely, justifying the fitting procedures as described in Section 3.

Using the temperature diagnostic obtained by the Fe XXIV and Fe XXIII line ratio in box 1, we can also provide a rough estimate of the electron number density N_e in the plasma by using the emission measure (EM_h) obtained from the AIA images in the 193 Å filter:

$$\mathrm{EM}_h = \frac{I_{\mathrm{obs}}}{R_{193\,\text{Å}}(T)}, \tag{8}$$

where I_{obs} is the observed averaged intensity of the AIA 193 Å image in box 1 at 15:59 UT, expressed in DN s^{-1}. $R_{193\,\text{Å}}(T)$ is the AIA response function in the 193 Å filter, which can be obtained by using the effective area provided by the SSW routine `aia_get_response.pro`, atomic data from CHIANTI v8 (Dere et al. 1997; Del Zanna et al. 2015), and photospheric abundances from Asplund et al. (2009), following the method described in the appendix of Del Zanna et al. (2011). Assuming the range of temperatures ($\log(T[\mathrm{K}]) \approx 7.3$–7.7) obtained from the Fe XXIV λ255.10/Fe XXIII λ263.76 ratio for Maxwellian and κ distributions, we obtain EM_h values varying between $5.2 \times 10^{31}\,\mathrm{cm}^{-5}$ and $1.8 \times 10^{32}\,\mathrm{cm}^{-5}$.

The plasma density can thus be estimated by using the following formula:

$$N_e \approx \sqrt{\frac{\mathrm{EM}_h}{N_H \times N_e \times h}}, \tag{9}$$

where h is depth of the plasma sheet, estimated by Warren et al. (2018) to be $\approx 10^{8.9}$ cm. The hydrogen density N_H can be expressed as $0.83N_e$ in a fully ionized gas with helium abundance relative to hydrogen $A(\mathrm{He}) = 0.1$. Using Equation (9) and the values of EM_h above, we obtain densities of the order of $(2.8\text{–}5.3) \times 10^{11}\ \mathrm{cm}^{-3}$ in the plasma sheet (at the location indicated by box 1 in Figure 2) during the impulsive phase of the 2017 September 10 flare. These densities can be directly compared with the values obtained from the analysis of the *RHESSI* spectra, as will be described in Section 5.

5. Analysis of *RHESSI* Data

RHESSI (Lin et al. 2002) started detecting the flare at $\approx$15:53 UT, while the very beginning of the flare was missed by the instrument, which was in the night part of its orbit. During the impulsive phase until $\approx$16:00 UT, the light curves of the HXR emission show several bursts up to $\sim$300 keV, whereas the emission at energies below $\sim$25 keV rises smoothly. We analyzed *RHESSI* spectra and images observed around 15:59 UT, when the EIS slit passed over the *RHESSI* HXR source. Despite that the thick attenuator, i.e., the A3 state, was in place at that time, the *RHESSI* data are still affected by pileup effects that distort the spectra formed in the $\approx$30–50 keV range. Currently, the pileup cannot be corrected for when

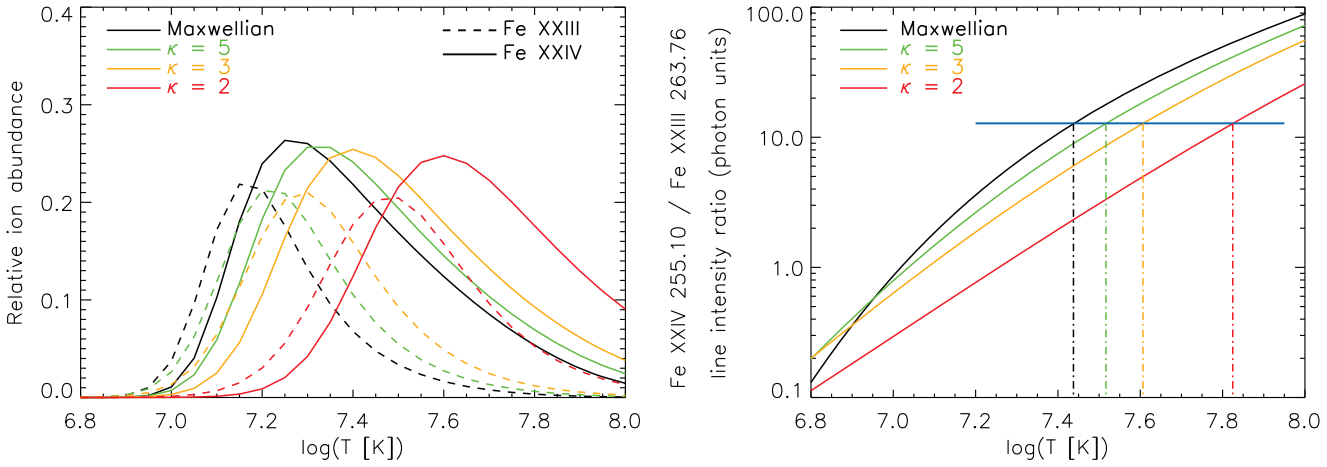

Figure 9. Left panel: fractional ion abundance for Fe XXIII and Fe XXIV for a Maxwellian distribution (black line) and non-Maxwellian distributions with different values of κ, as indicated in the legend. Right panel: theoretical Fe XXIV λ255.10/Fe XXIII λ263.76 ratio for electron Maxwellian (black line) and non-Maxwellian distributions with different values of κ, as indicated in the legend. The horizontal line indicates the observed ratio of 12.8 in box 1.

reconstructing the *RHESSI* images. Therefore, in Figure 2 the 30–50 keV energy range is omitted and the *RHESSI* sources are shown at energies below and above it. Figure 2 shows that the *RHESSI* sources are cospatial with the upper parts of the bright loops as seen, e.g., in the AIA 193 Å filter.

The *RHESSI* spectra were analyzed individually for detectors 3 and 8 (which seem to be less affected by pileup than detectors 1 and 6) and fitted within the 12–250 keV energy range. Energies below 12 keV were not included in the spectral analysis owing to an unknown instrumental effect modifying spectra in the A3 state. In order to take into account the pileup effects for the spectral analysis, `the (pileup_mod` fitting function was used. We analyzed the *RHESSI* spectrum accumulated during the time interval 15:59:04–15:59:16 UT, corresponding to the EIS box 1, in Figure 2.

The fits have revealed that a multi- or a double-thermal component dominating emission up to ~50 keV is needed to describe the *RHESSI* spectrum well. Both models are similar in terms of χ^2 and residuals. Fitting with a multithermal component, assuming that differential emission measure has a power-law dependence on temperature ($\sim T^{-\alpha}$), results in the following: a power-law index $\alpha \approx 6.3$, differential emission measure at $T = 23$ MK (2 keV) $DEM_{23} = 15 \times 10^{49}$ cm^{-3} kev^{-1}, and a maximum temperature $T_m = 55$–92 MK. On the other hand, the fit using a double-thermal component reveals the presence of a superhot component, $T_{sh} = 43$–56 MK, which dominates the HXR spectra in the ~18–30 keV energy range (see Figure 11). The *RHESSI* source reconstructed at this energy range is shifted toward higher coronal heights compared to the thermal source, $T = 21$ MK at lower energies 9–12 keV (see Figure 10), similarly to the superhot sources reported by Caspi & Lin (2010) and Caspi et al. (2015). The separation between thermal and superhot sources is rather small, around 1″–2″, but is seen consistently in all three different algorithms used for the image reconstruction (MEM NJIT, UV_Smooth, and VIS FWDFIT). Although source sizes and positions slightly differ between algorithms, the reconstructed *RHESSI* sources are similar in terms of modeled and observed modulation profiles and visibilities. We estimated a source area S and volume V from the 50% intensity contour of the reconstructed images, taking $V = 4/3\pi(S/\pi)^{3/2}$. Then, using the fitted emission measure of

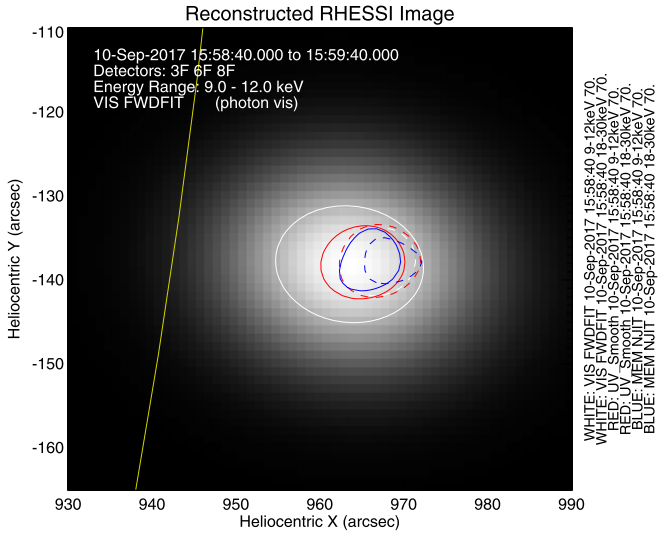

Figure 10. *RHESSI* sources in the 9–12 keV (full lines) and 18–30 keV (dashed lines) range reconstructed by three image algorithms: VIS FWDFIT (white), UV_Smooth (red), and MEM NJIT (blue). The background image is the VIS FWDFIT image in the 9–12 keV range. Contours are displayed at the 70% intensity level.

the thermal and superhot components, EM = (35–46) × 10^{49} cm^{-3} and EM_{sh} = (0.28–0.76) × 10^{49} cm^{-3}, and their volume, the electron density can be determined. The density of the thermal source is high, $N_e = (4.3–13) \times 10^{11}$ cm^{-3}, whereas the density of the superhot source is $N_{e,sh} = (0.86–2.2) \times 10^{11}$ cm^{-3}, again similarly to the one reported by Caspi & Lin (2010) for the 2002 July 23 X4.8 flare. These densities are consistent with the values (≈(2.8–5.3) × 10^{11} cm^{-3}) obtained in Section 4, using the estimated emission measure in the AIA 193 Å channel and temperature diagnostics from the EIS line ratio. Such a high-density source can be viewed as an example of the coronal thick-target source type discovered by Veronig & Brown (2004). Assuming source half-length $L = \sqrt{S/\pi}$ and the relation for the beam stopping energy $E_{stop} \approx \sqrt{10^{-17} nL}$ (e.g., Krucker & Lin 2008), the thermal source region is capable of collisional stopping of electrons of energies up to about 57–72 keV. Indeed, the

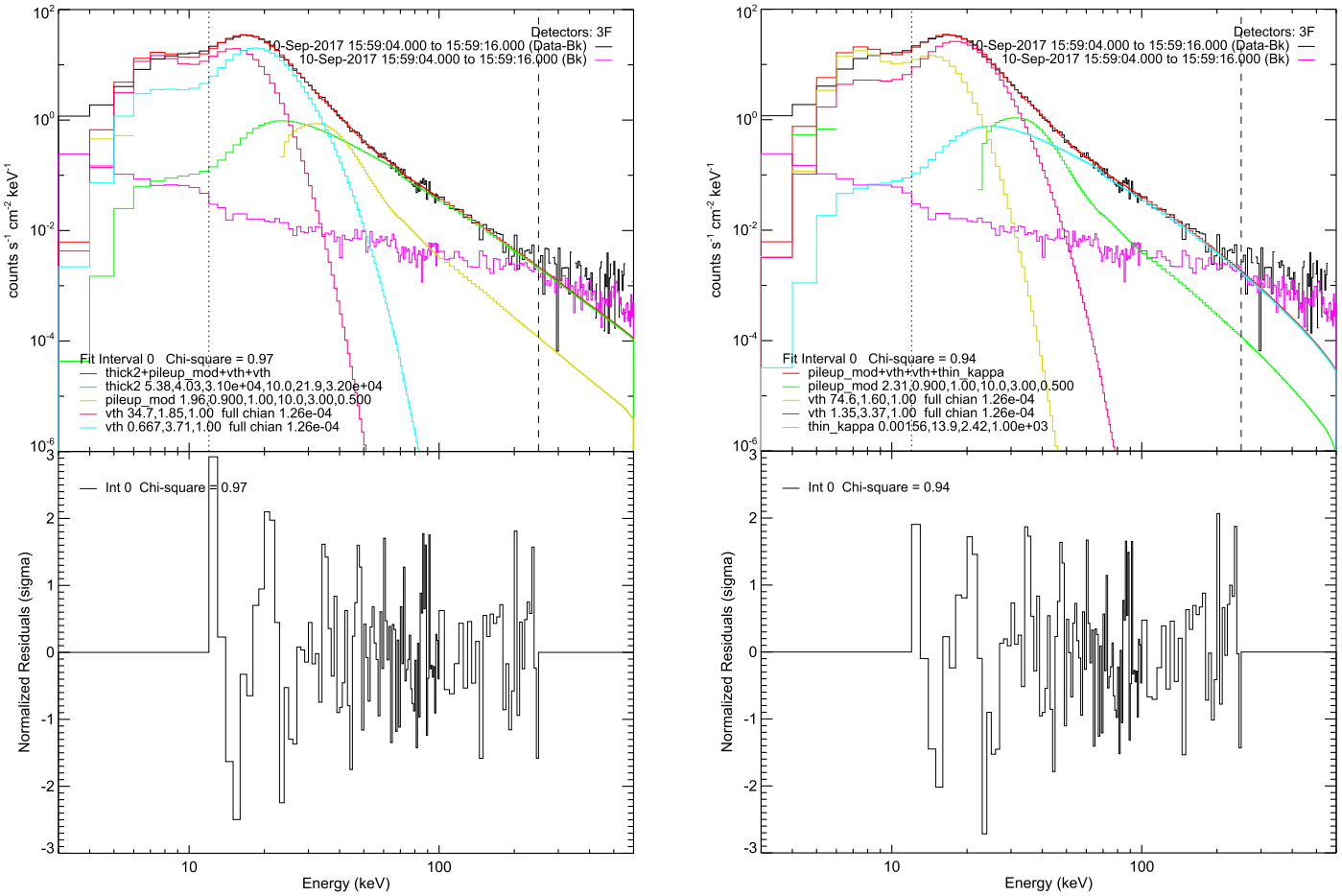

Figure 11. *RHESSI* spectra of 3F detector. Left: forward-fitted spectrum using two thermal components, vth, a correction for pileup effects, pileup_mod, and a thick-target power-law beam, thick2. Residua of the modeled and observed spectra are shown below the spectrum. Right: same as the left panel, but using a kappa distribution in the thin-target approximation, thin_kappa, instead of the thick-target beam component.

RHESSI loop-top source in the 50–100 keV range overlaps with the *RHESSI* thermal source and has a comparable size. However, we note that a *RHESSI* footpoint source in energies above 30 keV does exist (Gary et al. 2018). This could suggest that the footpoint source might not be in the same loop/magnetic field as the loop-top source.

Given the nature of *RHESSI* sources, a thick-target component at energies above ∼50 keV was used in spectral analysis of spatially integrated *RHESSI* spectra. The observed *RHESSI* spectrum can be fitted with an injected electron power-law beam of $\delta \approx 4$, which is significantly harder than the values reported by Veronig & Brown (2004). Although the *RHESSI* source in the 100–300 keV range overlaps with the thermal source, it has a more elongated shape and cannot be interpreted as a thick-target region for electrons of such energies. Using the half-length measured across the 50% intensity contour, the stopping energy is in the 77–130 keV range. Therefore, it is also relevant to use the thin-target approximation. Figure 11 shows such an example for a thin-target κ distribution (see Kašparová & Karlický 2009; Oka et al. 2013). Further, the spectra can be fitted with a thin-target power-law beam equally well in terms of χ^2 and residuals. While the power-law index thus obtained is ≈2.5, κ ranges between 2.1 and 2.4. These values are consistent with the ones derived for ions from the EIS line fitting (Section 3).

Note that at energies below 50 keV the *RHESSI* spectrum can be fitted by a single kappa distribution instead of two thermal components. Although such a component has fewer free parameters, due to the different source sizes and positions in the energy ranges 9–12 keV and 18–30 keV where each of the thermal components dominates, we excluded such a fitting function as inappropriate. Finally, the *RHESSI* spectrum cannot be fitted well enough with two components only, e.g., with a thermal component and a beam single power-law/κ component (as in Oka et al. 2015). A reasonable fit can also be obtained for a double power-law beam with a steep (soft) spectrum above ∼70 keV only, i.e., mimicking the nature of a multi- or double-thermal component. Such a fit was not interpreted as more appropriate.

6. Discussion and Interpretation

We now proceed to discuss the possible interpretation of the observed line profiles and *RHESSI* spectra.

Jeffrey et al. (2016) listed three possible interpretations to the observed κ emission line profiles in solar flares:

1. plasma is multithermal along the line of sight;
2. Fe ions are accelerated isotropically to a non-Maxwellian distribution of velocities; and
3. turbulence is present, in terms of macroscopic parameters (T, n_e, or velocities).

We shall deal with these in the following subsections.

6.1. Multithermal Plasmas

Interpretation 1 is based on the fact that any non-Maxwellian distribution with a thermal core and a tail can be represented by a linear combination of Maxwellians with different temperatures. For a κ-distribution, this Maxwellian decomposition and its coefficients were provided by Hahn & Savin (2015). In terms of the line profile fitting, one should fit a series of Gaussians to the line profile, each representing a Maxwellian at a given temperature. We have seen in Section 3.1 that such fitting is unconstrained, with the exception shown in the right panel of Figure 4. Using the widths of such a double-Gaussian fit, $w_{G1,2}$, we obtain equivalent ion temperatures $T_{G1,2}$ (also called Doppler temperatures) by using the formula (compare Equations (8) and (10) of Dudík et al. 2017b)

$$w_G^2 - w_{instr}^2 = \frac{k_B T_G}{m_{Fe}} \frac{\lambda_0^2}{c^2}, \quad (10)$$

where we subtracted the w_{instr}^2 factor to account for the instrumental broadening. Equation (10) yields $T_{G1,2} = 62$ and 99 MK for the two Gaussians, respectively. Both are significantly higher (by factors of ≈2.3 and 3.6) than the corresponding T_e derived from the Fe XXIV/Fe XXIII line intensity ratio (Section 4). If the plasma were really multithermal with dominant temperature components at T_{G1} and T_{G2} (assuming equilibrium between electrons and ions), the T_e obtained should be correspondingly higher. Since it is not, we suggest that the multithermal interpretation is not likely.

6.2. Accelerated Ions

Interpretation 2, namely that ions are accelerated, is in line with recent theoretical modeling of Li et al. (2017), who showed that ions can be accelerated preferentially to electrons in flare conditions. That the ion profiles could be due to accelerated ions has also been thoroughly examined by Jeffrey et al. (2017), who used the formulae derived by and adapted from Sigmar & Joyce (1971) and Stix (1972) to calculate the thermalization time for accelerated ions, in their case, Fe XVI and Fe XXIII. The thermalization timescale τ_f was derived to be $\approx 10^{-2}$ s. In our case, using the values of $N_e = 5 \times 10^{11}$ cm^{-3} and T_e derived in Section 4, the corresponding ion thermalization timescales would be even shorter by about two orders of magnitude.

However, we note that Equation (13) of Jeffrey et al. (2017) is applicable only for ion velocities v satisfying $v_{th,i} \ll v \ll v_{th,e}$, where v_{th} are ion and electron thermal speeds, equal to $\sqrt{2k_B T_{e,i}/m_{e,i}}$, respectively. In our case, the condition $v_{th,i} \ll v$ is broken: If we suppose that the ions are accelerated to a κ-distribution corresponding to $\kappa \approx 2$ profiles shown in Figure 3, we obtain, as an order-of-magnitude estimate, Doppler velocities $v \approx 300$ km s^{-1} for the far wings of the Fe XXIV λ255.1 line at $\Delta\lambda \approx 0.25$ Å, since $\Delta\lambda/\lambda_0 = v/c$. If we assume that the ions have the same temperature as electrons, i.e., $\log(T_e[K]) = 7.4$–7.8 derived in Section 4, we obtain ion thermal velocities of 90–140 km s^{-1}, i.e., of the same order of magnitude. Thus, Equation (13) of Jeffrey et al. (2017) for calculation of ion thermalization timescales may not be entirely applicable in our case.

Jeffrey et al. (2017) invoked the results of Bian et al. (2014) to conclude that if the line profiles are due to accelerated ions, then the ions must be accelerated locally and continuously during the flare. This conclusion is based on the fact that, according to Bian et al. (2014), the κ^* index (with $\kappa^* = \kappa + 1$; Livadiotis & McComas 2009, see Sections 3 and 4.1 therein) is a parameter describing the ratio of the competing acceleration and collisional timescales, $\kappa^* = \tau_{acc}/2\tau_{coll}$. Such a conclusion is natural, since the short ion thermalization timescales mean that if the acceleration process is turned off, the ions thermalize much faster compared to EIS exposure times; therefore, if non-Gaussian lines are observed, the acceleration process must persist.

If our line profiles are also due to accelerated ions, then the conclusion of Jeffrey et al. (2017) is again valid and straightened in terms of acceleration being both local and continuous. This is because in our case the ion thermalization timescales are even shorter, while we get similar values of κ^*. Since the thermalization timescale is proportional to τ_{coll} and $\tau_{coll} = \tau_{acc}/2\kappa^*$, and since the thermalization length $L_f = v\tau_f$ is proportional to the product of ion velocity and thermalization timescale, our smaller thermalization timescale (compared to Jeffrey et al. 2017) means both shorter acceleration timescales and shorter thermalization lengths.

We also emphasize that similar κ values were found for the ion (from the EIS Fe XXIV line profiles) and electron (from *RHESSI*) distributions. This consistency suggests that the ions were accelerated and that the acceleration process produced both fast electrons and ions with similar distribution functions.

To summarize, the interpretation that ions are accelerated locally and continuously during the flare remains a valid candidate for our observation.

6.3. Turbulence

Macroscopic turbulence is often invoked as an explanation for the nonthermal line widths, i.e., widths larger than the corresponding thermal ones given by Equation (10). The reasons for the invocation of turbulence in flare observations are well described, e.g., in Section 3 of the review of Antonucci (1989). One typical example is given by the observation of large nonthermal widths in the spectra of blueshifted high-temperature lines during chromospheric evaporation, which are often explained in terms of turbulent mass motions, or alternatively superposition of unresolved flows (e.g., Milligan 2011; Polito et al. 2015).

Rather than chromospheric evaporation, the nonthermal broadening could also be related to HXR emission during flares, as the onset of nonthermal broadening occurs simultaneously with detection of low-intensity HXR emission and can even precede the strong HXR bursts (e.g., Antonucci 1989). Alternatively, the nonthermal broadening could be associated with redshifts (due to small bulk downflows), as reported by Jeffrey et al. (2017), which could drive turbulence. In our case, it is difficult to establish the presence of true downflows along the flaring structures owing to the off-limb geometry and the uncertainty of the EIS wavelength calibration (Kamio et al. 2010).

The observed consistency of nonthermal broadenings observed in lines of ions of different elements (e.g., Doschek et al. 1979, Table 1 therein) and the absence of variation with the flare position on the disk or limb (in contrast to what is expected by assuming that the broadening is caused by superposition of flows) were also used as arguments in favor

of turbulent (random) motions. Further, in these early studies, large differences between equivalent ion temperatures and electron temperatures derived from line ratios were observed for several minutes (e.g., Antonucci 1989), suggesting that the broadening could not be caused by an effective ion–electron temperature difference, as this could not be maintained for such a long timescale.

But is this line of reasoning valid in our case? To test this, we first estimate the equivalent ion temperatures for the ion κ-distributions corresponding to the observed line profiles. We take the value of $w_\kappa = 0.15$ Å for the Fe XXIV line at 255.1 Å from Figure 3 and calculate the equivalent T_κ using the formula (compare Equations (6) and (11) of Dudík et al. 2017b)

$$w_\kappa^2 = \frac{k_B T_\kappa}{m_{Fe}} \frac{\lambda_0^2}{c^2}. \quad (11)$$

Note that the w_κ and w_G were derived to have the same physical meaning as if interpreted in terms of the equivalent ion temperature. This stems from the temperature having the same physical meaning for a Maxwellian and a κ-distribution. We also note that, unlike for w_G (Equation (10)), the instrumental width is already accounted for since the fit is a convolution (see Equation (1)). Using the above formula, we obtain T_κ=205 ± 22 MK, or $\log(T_\kappa[K]) \approx 8.3$. Similarly, for the lowest value of $w_\kappa = 0.10$ (Figure 4), we would still obtain $T_\kappa = 99 \pm 3$ MK. The uncertainties in these temperatures are calculated using the corresponding uncertainties of w_κ.

An estimate of the upper limit on the uncertainty of T_e derived from the Fe XXIV/Fe XXIII line intensity ratio can be obtained by assuming that both the Fe XXIV λ255.1 and Fe XXIII λ263.8 line intensities contain not only the photon noise uncertainty but also the ≈20% calibration uncertainty (Culhane et al. 2007), despite these lines being both observed in the LW channel of EIS. Doing so would yield electron temperatures of 27 ± 4 MK assuming Maxwellian, 39 ± 7 MK for $\kappa = 3$, and 66 ± 10 MK for $\kappa = 2$, respectively. We emphasize that in general assuming that the ions are formed under non-Maxwellian conditions results in a higher formation temperature (and thus broader thermal widths) than expected in Maxwellian conditions. In turn, this decreases the amount of nonthermal width that needs to be invoked to explain the observed profiles. Nevertheless, the temperatures listed above are still too low compared to the equivalent ion temperatures that are required to explain the observed large widths in this work. The conclusion is thus that turbulence is still a possible explanation for the observed line widths w_κ and the non-Gaussian κ profiles. We note that if the turbulent diffusion coefficient is inversely proportional to velocity, a κ-distribution is formed (Bian et al. 2014).

Thus, we estimate the "nonthermal" widths w_{nth} for the non-Gaussian profiles. To a first approximation, this can be done by setting (see Dudík et al. 2017b)

$$w_{nth}^2 = w_\kappa^2 - w_{th}^2. \quad (12)$$

This equation is not exact; rather, it gives a lower limit of the w_{nth}. This is since a convolution of two κ-distributions with the same κ but different w_{th} and w_{nth} is *not* a κ-distribution of the same κ. This arises from the fact that a sum is present in the $(1 + (\lambda - \lambda_0)^2/2\kappa w^2)^{-\kappa}$ subintegral functions. However, the resulting convolution is slightly wider, but not too different from those obtained using approximation (12).

For the fit results from Figure 4, i.e., $\kappa \approx 3$, $w_\kappa = 0.10$, we obtain for $T = 39$ MK that $w_{th} = 0.065$ Å, from which subsequently $w_{nth} = 0.076$ Å (or ≈126 km s^{-1}), a factor of ≈1.2 larger than w_{th}. Similarly, for the fit results of Figure 3, i.e., $\kappa \approx 2$, $w_\kappa = 0.15$, we obtain for $T = 66$ MK that $w_{th} = 0.085$ Å, from which subsequently $w_{nth} = 0.124$ Å (or ≈205 km s^{-1}), again a factor of ≈1.5 larger than the corresponding w_{th}.

We note that the nonthermal velocity of 205 km s^{-1} is among the largest reported in flares, being even higher than the value of ≈160 km s^{-1} reported from X-ray and EUV spectra (e.g., Doschek et al. 1979, 1980; Feldman et al. 1980; Antonucci et al. 1982; Antonucci 1989; Landi et al. 2003; Del Zanna 2008). To our knowledge, there are not many reports of higher nonthermal velocities. For example, Tanaka et al. (1982, Figure 3 therein) reported such velocities from Fe XXVI spectra (but not Fe XXV), decreasing from 250 km s^{-1} during the course of their flare. Antonucci et al. (1986) reported velocities of 220 km s^{-1}. At present, similar nonthermal line widths were seen with EIS in the Fe XXIII line previously by Lee et al. (2017, see their Figure 9).

6.4. Superhot Ions Due to Collisions with High-energy Electrons?

Finally, we turn our attention to a possible explanation not considered by Jeffrey et al. (2016, 2017), which is that the κ distributions might be caused by collisions of superhot ions with high-energy electrons. This scenario is suggested by the fact that the high-energy tail in the *RHESSI* spectra could be fitted with a κ-distribution with κ values of 2.1–2.4 (Section 5), which are similar to the ones obtained from some line profiles (see, e.g., Figures 3 and 8). Although the fitting of the high-energy tail observed by *RHESSI* yields a well-constrained κ, the corresponding temperatures are not well constrained. This is due to the fact that the quasi-thermal core of such a κ-distribution occurs at low energies, of about ≈20–30 keV (cyan line in the top right panel of Figure 11), where the spectrum is dominated by the thermal components and pileup. We determined that electron temperatures of about 20–160 MK are still compatible with the observed high-energy tail, without an appreciable change in the χ^2 and residuals of the *RHESSI* spectrum fit. In fact, the top right panel of Figure 11 shows a fit using a temperature of 14 keV, equivalent to about 160 MK. These temperatures are comparable, at least to within an order of magnitude, to the equivalent ion temperatures T_κ derived in Section 6.3.

Could such temperatures be realistic? In the 2D particle-in-cell simulation of Karlický & Bárta (2011), electron temperatures of 60–120 MK are reached during merging of plasmoids occurring as a result of tearing instability in the current sheet. In addition, the velocity distribution could show high-energy tails, although details depend on the location (see Figure 6 in Karlický & Bárta 2011). Such a process could possibly occur within our flare, and we note that the locations of the observed non-Gaussian lines (Figure 8), i.e., the top of the flare arcade and in the plasma sheet feature, would both be appropriate with respect to the geometry of Karlický & Bárta (2011), as plasmoids can also impact the top of the flare arcade and merge with it (see, e.g., Jelínek et al. 2017).

For the above reasons, as well as the fact that the *RHESSI* thermal coronal source is thick-target for energies $\lesssim$57–72 keV (Section 5), we proceed to speculate whether the high equivalent ion temperatures could be due to the impact of these high-energy $\kappa = 2$ electrons. We first calculate the electron thermalization time due to collisions with both electrons and ions, using Equation (3.50) of Goedbloed & Poedts (2004),

$$\tau_e \approx \frac{1.09 \times 10^{10}}{\ln\Lambda} \frac{\widetilde{T_e}^{3/2}}{Z_f N_e}, \quad (13)$$

with $T_e = 3$ keV ($\approx$35 MK) and $N_e = 5 \times 10^{11}$ cm^{-3}, where $\ln\Lambda \approx 10$ is the Coulomb logarithm, $\widetilde{T_e}$ is electron temperature in keV, N_e is electron number density in cm^{-3}, and Z_f is the charge of ions involved, which we take to be $Z_f = 1$. Note that the τ_e scales with $\widetilde{T_e}^{3/2}$ owing to the fact that progressively higher-energy electrons are less collisional. Considering now that the background plasma impacted by the beam has $\widetilde{T_e} =$ 3 keV and $N_e \approx 5 \times 10^{11}$ cm^{-3}, we obtain $\tau_e = 8 \times 10^{-3}$ s. The corresponding electron–ion temperature equilibration time, i.e., the time at which electrons and ions reach thermal equilibrium with the same temperature, is longer by a factor of $m_i/2m_e$ (see Equation (3.55) of Goedbloed & Poedts 2004). Considering the Fe ions, we obtain that the temperature equilibration time is $\approx$388 s.

Therefore, in principle, if the electron beam persists for such timescales, the ions could possibly be heated by impacting electrons to temperatures of the electron high-energy tail. However, we remind the reader that the temperature of the $\kappa \approx 2$ high-energy tail is not well constrained from *RHESSI*.

Finally, we estimate the amount of energy that could be transferred to the ions from the impacting high-energy electron tail. To do so, we calculate the amount δE_e of the energy contained in the tail. This can be done by integrating the corresponding *RHESSI* spectral component, resulting in $\delta E_e/\delta t = 3.7 \times 10^{28}$ erg s^{-1}. The corresponding temperature gain by particular ions can then be estimated as

$$\Delta T_i \sim \frac{\delta E_e}{\delta t} \frac{\Delta t A_{Fe}}{N_e V k_B}, \quad (14)$$

where Δt is the duration of the high-energy tail, A_{Fe} is the iron abundance, and V is the ambient volume, where the energy exchange occurs. Using the photospheric value of $A_{Fe} \approx 3.2 \times 10^{-5}$ (Asplund et al. 2009), estimating V from the size of the *RHESSI* thermal source at 9–12 keV as $V \approx 2.7 \times 10^{26}$ cm^3, and using $\Delta t = 11$ minutes as an upper-limit estimate from the *Fermi* light curves (see also Long et al. 2018), we obtain $\Delta T_i = 0.05$ MK. This value is too low for ambient ions to be efficiently heated by the high-energy electron tail. The value could be increased only by considering that the ambient volume V is much smaller; however, decreasing it by even two orders of magnitude would still produce inefficient heating. We therefore conclude that this mechanism is not a likely explanation of the observed ion emission line profiles.

7. Summary

We reported on the *Hinode*/EIS observations of wide and non-Gaussian profiles of Fe XXIV EUV lines during the impulsive phase of the 2017 September 10 X8.3-class solar flare. These lines are the hottest observed by EIS. We speculate that such a strong departure from Gaussian profiles in the high-temperature lines could be observed in this large flare event (and not in previous X-class flares observed by EIS) thanks to the combination of (1) very intense line profiles, with wings that could be properly fitted; (2) the ideal location of the flare on the limb, which allowed us to observe the high-temperature emission in the plasma sheet without contamination from the loop emission; and (3) the favorable position of the EIS slit above the flare loops.

The profiles of the Fe XXIV lines could be reliably fitted with a κ-distribution with low values of κ, in the range of $\approx$1.7–3.3. Different κ-values provide information about the number of particles in the high-energy tail (see, e.g., Oka et al. 2013, Figure 1). For instance, an electron distribution with $\kappa = 2$ means that $\approx$35% of the particles are accelerated and they carry >80% of the energy. The non-Gaussian line profiles were found in the location of the top of the flare arcade as observed by *SDO*/AIA in boxes 1 and 2 of Figure 2, at the bottom and along the plasma sheet feature at about 15:59 UT, respectively. The location in box 1 is coincident with the maximum intensity of the *RHESSI* thermal and nonthermal sources at energies of 6–300 keV and is consistent with the location of the EOVSA microwave gyrosynchrotron source at the high-frequency end.

In all the observed profiles, single κ fits of the Fe XXIV λ255.10 line perform significantly better than single-Gaussian fits. On the other hand, the pronounced wings of the Fe XXIV λ192.06 line profiles can in principle be approximated by multiple-Gaussian fits. However, with only a singular exception, such fits are unconstrained. For the Fe XXIV λ255.1 line, this is at least in part due to it red wing occurring outside of the corresponding wavelength windows. Nevertheless, a multiple-Gaussian fit gives a width for the dominant Fe XXIV λ192.06 component that is unrealistically narrower ($w_G = 0.10 \pm 0.005$ Å or FWHM$_G = 0.21 \pm 0.04$ Å) than the one obtained in the same location for the other Fe XXIV line at 255.10 Å ($w_G = 0.13 \pm 0.009$ Å or FWHM$_G =$ 0.31 ± 0.02 Å).

Considering different possibilities, we show that the observed non-Gaussian line profiles could be due to either local and continuous ion acceleration or turbulence. This conclusion is in agreement with Jeffrey et al. (2017). The explanation due to multithermal plasma is unlikely, as the equivalent ion temperatures required by the double-Gaussian fits are unrealistically large. Similarly, although the line profiles have similar κ to the *RHESSI* high-energy tail, as well as possibly similar temperatures, it is unlikely that the electron beam heats these ions, as the energy content of the beam is too weak.

We note that the κ parameter for electrons cannot be diagnosed from line intensities using the ratio–ratio method (see Dudík et al. 2014; Dudík et al. 2015). We could only use the temperature-sensitive Fe XXIV/Fe XXIII line intensity ratio to diagnose the T_e if a value of κ was assumed. This theoretical temperature-sensitive ratio is shifted to larger T_e for low κ, a consequence of the behavior of the ionization equilibrium. Using the observed Fe XXIV/Fe XXIII ratio, we obtain $T_e = 27$ MK if a Maxwellian distribution is assumed, while for $\kappa = 3$ the

temperature reaches 39 MK, and for $\kappa = 2$ it reaches 66 MK. Although this effect leads to an increase of the corresponding thermal velocity for the low κ values determined from line profiles or the *RHESSI* high-energy tail, the line profiles are still broad enough to indicate that the approximate lower limit of the nonthermal velocities, if interpreted in terms of turbulence, can be larger than 200 km s^{-1}.

We conclude that the nonthermal widths, long observed at the start and impulsive phases of solar flares, are likely connected with extremely non-Gaussian line profiles of the hottest Fe lines, which could be detected here owing to good wavelength coverage and resolution of EIS. The present observations of the wide non-Gaussian profiles and HXR/microwave loop-top sources, along with the favorable limb geometry of our flare, provide important observational constraints into the mechanisms responsible for the energy release in the impulsive phase of large solar flares.

The authors acknowledge helpful discussions with M. Karlický, G. Del Zanna, and H. E. Mason. J.K. would like to thank the *RHESSI* team, namely, K. Tolbert, B. Dennis, S. Krucker, and R. Schwartz, for their invaluable advice and software support. V.P. is supported by NASA grant NNX15AF50G, grant no. 2015-065 from the University of Alabama in Huntsville, and contract 8100002705 from Lockheed-Martin to SAO. P.T. acknowledges support by NASA grant NNX15AF50G, contract 8100002705 from Lockheed-Martin to SAO, and contract NNM07AB07C to SAO.

J.D., J.K., and E.D. acknowledge support from grant nos. 17-16447S and 18-09072S of the Grant Agency of the Czech Republic, as well as institutional support RVO:67985815 from the Czech Academy of Sciences. B.C. acknowledges support by NASA grant NNX17AB82G and NSF grant AGS-1654382. V.P., J.K., and K.K.R. would like to thank the International Space Science Institute (ISSI) for their support and hospitality during the meetings of the ISSI Bern-Beijing team on "Diagnosing heating mechanisms in solar flares through spectroscopic observations of flare ribbons." AIA data are courtesy of NASA/*SDO* and the AIA science team. *Hinode* is a Japanese mission developed and launched by ISAS/JAXA, with NAOJ as domestic partner and NASA and STFC (UK) as international partners. It is operated by these agencies in cooperation with ESA and NSC (Norway). CHIANTI is a collaborative project involving the NRL (USA), the University of Cambridge (UK), and George Mason University (USA).

Facilities: Hinode, *SDO*, *RHESSI*, EOVSA.

ORCID iDs

Jaroslav Dudík https://orcid.org/0000-0003-1308-7427
Katharine K. Reeves https://orcid.org/0000-0002-6903-6832
Paola Testa https://orcid.org/0000-0002-0405-0668
Bin Chen https://orcid.org/0000-0002-0660-3350

References

Antonucci, E. 1989, SoPh, 121, 31
Antonucci, E., Gabriel, A. H., Acton, L. W., et al. 1982, SoPh, 78, 107
Antonucci, E., Rosner, R., & Tsinganos, K. 1986, ApJ, 301, 975
Asplund, M., Grevesse, N., Sauval, A. J., & Scott, P. 2009, ARA&A, 47, 481
Bamba, Y., Lee, K.-S., Imada, S., & Kusano, K. 2017, ApJ, 840, 116
Battaglia, M., & Kontar, E. P. 2013, ApJ, 779, 107
Battaglia, M., Motorina, G., & Kontar, E. P. 2015, ApJ, 815, 73
Bian, N. H., Emslie, A. G., Stackhouse, D. J., & Kontar, E. P. 2014, ApJ, 796, 142
Boerner, P., Edwards, C., Lemen, J., et al. 2012, SoPh, 275, 41
Brooks, D. H., & Warren, H. P. 2016, ApJ, 820, 63
Brosius, J. W. 2013, ApJ, 777, 135
Caspi, A., & Lin, R. P. 2010, ApJL, 725, L161
Caspi, A., Shih, A. Y., McTiernan, J. M., & Krucker, S. 2015, ApJL, 811, L1
Che, H., & Goldstein, M. L. 2014, ApJL, 795, L38
Culhane, J. L., Harra, L. K., James, A. M., et al. 2007, SoPh, 243, 19
Culhane, J. L., Rapley, C. G., Bentley, R. D., et al. 1981, ApJL, 244, L141
De Pontieu, B., McIntosh, S., Martinez-Sykora, J., Peter, H., & Pereira, T. M. D. 2015, ApJL, 799, L12
De Pontieu, B., Title, A. M., Lemen, J. R., et al. 2014, SoPh, 289, 2733
Del Zanna, G. 2008, A&A, 481, L69
Del Zanna, G. 2012, A&A, 537, A38
Del Zanna, G. 2013, A&A, 555, A47
Del Zanna, G., Berlicki, A., Schmieder, B., & Mason, H. E. 2006, SoPh, 234, 95
Del Zanna, G., Dere, K. P., Young, P. R., Landi, E., & Mason, H. E. 2015, A&A, 582, A56
Del Zanna, G., O'Dwyer, B., & Mason, H. E. 2011, A&A, 535, A46
Dere, K. P., Landi, E., Mason, H. E., Monsignori Fossi, B. C., & Young, P. R. 1997, A&As, 125, 149
Doschek, G. A., Feldman, U., Kreplin, R. W., & Cohen, L. 1980, ApJ, 239, 725
Doschek, G. A., Kreplin, R. W., & Feldman, U. 1979, ApJL, 233, L157
Dudík, J., Del Zanna, G., Mason, H. E., & Dzifčáková, E. 2014, A&A, 570, A124
Dudík, J., Dzifčáková, E., Meyer-Vernet, N., et al. 2017a, SoPh, 292, 100
Dudík, J., Mackovjak, Š, Dzifčáková, E., et al. 2015, ApJ, 807, 123
Dudík, J., Polito, V., Dzifčáková, E., Del Zanna, G., & Testa, P. 2017b, ApJ, 842, 19
Dudík, J., Polito, V., Janvier, M., et al. 2016, ApJ, 823, 41
Dzifčáková, E., Dudík, J., Kotrč, P., Fárník, F., & Zemanová, A. 2015, ApJS, 217, 14
Dzifčáková, E., Zemanová, A., Dudík, J., & Mackovjak, Š 2018, ApJ, 853, 158
Feldman, U., Doschek, G. A., Kreplin, R. W., & Mariska, J. T. 1980, ApJ, 241, 1175
Fletcher, L., Dennis, B. R., Hudson, H. S., et al. 2011, SSRv, 159, 19
Freeland, S. L., & Handy, B. N. 1998, SoPh, 182, 497
Gary, D. E., Chen, B., Dennis, B. R., et al. 2018, arXiv:1807.02498
Goedbloed, J. P. H., & Poedts, S. 2004, Principles of Magnetohydrodynamics (Cambridge: Cambridge Univ. Press)
Gontikakis, C., Patsourakos, S., Efthymiopoulos, C., Anastasiadis, A., & Georgoulis, M. K. 2013, ApJ, 771, 126
Gordovskyy, M., Browning, P. K., Kontar, E. P., & Bian, N. H. 2013, SoPh, 284, 489
Gordovskyy, M., Browning, P. K., Kontar, E. P., & Bian, N. H. 2014, A&A, 561, A72
Hahn, M., & Savin, D. W. 2015, ApJ, 809, 178
Hasegawa, A., Mima, K., & Duong-van, M. 1985, PhRvL, 54, 2608
Jeffrey, N. L. S., Fletcher, L., & Labrosse, N. 2016, A&A, 590, A99
Jeffrey, N. L. S., Fletcher, L., & Labrosse, N. 2017, arXiv:1701.02196
Jeffrey, N. L. S., Hahn, M., Savin, D. W., & Fletcher, L. 2018, ApJL, 855, L13
Jelínek, P., Karlický, M., Van Doorsselaere, T., & Bárta, M. 2017, ApJ, 847, 98
Kamio, S., Hara, H., Watanabe, T., Fredvik, T., & Hansteen, V. H. 2010, SoPh, 266, 209
Karlický, M., & Bárta, M. 2011, ApJ, 733, 107
Kašparová, J., & Karlický, M. 2009, A&A, 497, L13
Kosugi, T., Matsuzaki, K., Sakao, T., et al. 2007, SoPh, 243, 3
Krucker, S., Battaglia, M., Cargill, P. J., et al. 2008, A&Ar, 16, 155
Krucker, S., & Lin, R. P. 2008, ApJ, 673, 1181
Laming, J. M., & Lepri, S. T. 2007, ApJ, 660, 1642
Landi, E., Feldman, U., Innes, D. E., & Curdt, W. 2003, ApJ, 582, 506
Lee, K.-S., Imada, S., Watanabe, K., Bamba, Y., & Brooks, D. H. 2017, ApJ, 836, 150
Lemen, J. R., Title, A. M., Akin, D. J., et al. 2012, SoPh, 275, 17
Li, D., Li, Y., Su, W., Huang, Y., & Ning, Z. 2018, ApJ, 854, 26
Li, X., Guo, F., Li, H., & Li, G. 2017, ApJ, 843, 21
Lin, R. P., Dennis, B. R., Hurford, G. J., et al. 2002, Sol. Phys., 210, 3
Liu, W., Meng, J., Cooper, D., et al. 2018, arXiv:1807.09847
Livadiotis, G. 2017, Kappa Distributions: Theory and Applications in Plasmas (Amsterdam, Netherlands: Elsevier)
Livadiotis, G., & McComas, D. J. 2009, JGRA, 114, 11105
Long, D. M., Harra, L. K., Matthews, S. A., et al. 2018, ApJ, 855, 74

Milligan, R. O. 2011, ApJ, 740, 70
Oka, M., Ishikawa, S., Saint-Hilaire, P., Krucker, S., & Lin, R. P. 2013, ApJ, 764, 6
Oka, M., Krucker, S., Hudson, H. S., & Saint-Hilaire, P. 2015, ApJ, 799, 129
Olbert, S. 1968, in Astrophysics and Space Science Library, Vol. 10, Physics of the Magnetosphere, ed. R. D. L. Carovillano & J. F. McClay (Dordrecht: Reidel), 641
Pesnell, W. D., Thompson, B. J., & Chamberlin, P. C. 2012, SoPh, 275, 3
Polito, V., Reep, J. W., Reeves, K. K., et al. 2016, ApJ, 816, 89
Polito, V., Reeves, K. K., Del Zanna, G., Golub, L., & Mason, H. E. 2015, ApJ, 803, 84
Schmieder, B., Aulanier, G., & Vršnak, B. 2015, SoPh, 290, 3457
Seaton, D. B., & Darnel, J. M. 2018, ApJL, 852, L9
Sigmar, D., & Joyce, G. 1971, NucFu, 11, 447
Stix, T. H. 1972, PlPh, 14, 367
Tanaka, K., Watanabe, T., Nishi, K., & Akita, K. 1982, ApJL, 254, L59
Testa, P., De Pontieu, B., & Hansteen, V. 2016, ApJ, 827, 99
Tian, H., Li, G., Reeves, K. K., et al. 2014, ApJL, 797, L14
Vasyliunas, V. M. 1968a, JGR, 73, 2839
Vasyliunas, V. M. 1968b, in Astrophysics and Space Science Library, Vol. 10, Physics of the Magnetosphere, ed. R. D. L. Carovillano & J. F. McClay (Dordrecht: Reidel), 622
Veronig, A. M., & Brown, J. C. 2004, ApJL, 603, L117
Vocks, C., Dzifčáková, E., & Mann, G. 2016, A&A, 596, A41
Vocks, C., Mann, G., & Rausche, G. 2008, A&A, 480, 527
Warren, H. P., Brooks, D. H., Ugarte-Urra, I., et al. 2018, ApJ, 854, 122
Warren, H. P., Ugarte-Urra, I., & Landi, E. 2014, ApJS, 213, 11
Woods, M. M., Harra, L. K., Matthews, S. A., et al. 2017, SoPh, 292, 38
Yan, X. L., Yang, L. H., Xue, Z. K., et al. 2018, ApJL, 853, L18
Young, P. R., Doschek, G. A., Warren, H. P., & Hara, H. 2013, ApJ, 766, 127
Young, P. R., Tian, H., & Jaeggli, S. 2015, ApJ, 799, 218